

Full length article

Inherent and multiple strain hardening imparting synergistic ultrahigh strength and ductility in a low stacking faulted heterogeneous high-entropy alloy



Zibing An^a, Shengcheng Mao^{a,*}, Yinong Liu^{b,*}, Luyan Yang^{a,c}, Ashok Vayyala^{c,d}, Xiao Wei^e, Cheng Liu^e, Caijuan Shi^f, Huixin Jin^{a,g}, Cuixiu Liu^a, Jianxin Zhang^g, Ze Zhang^{a,e}, Xiaodong Han^{a,*}

^a Beijing Key Laboratory of Microstructure and Property of Advanced Materials, Faculty of Materials and Manufacturing, Beijing University of Technology, Beijing 100124, PR.China

^b Department of Mechanical Engineering, The University of Western Australia, Perth, WA, 6009, Australia

^c Ernst Ruska-Centre for Microscopy and Spectroscopy with Electrons, Forschungszentrum Jülich GmbH, 52425 Jülich, Germany

^d Central Facility for Electron Microscopy (GFE), RWTH Aachen University, Ahornstr. 55, 52074 Aachen, Germany

^e Center of Electron Microscopy, State Key Laboratory of Silicon Materials, School of Materials Science and Engineering, Zhejiang University, Hangzhou 310058, China

^f Institute of High Energy Physics, Chinese Academy of Sciences, Beijing, 100049, PR.China

^g School of Materials Science & Engineering, Shandong University, Shandong, 250100, China

ARTICLE INFO

Article history:

Received 13 September 2022

Revised 7 November 2022

Accepted 11 November 2022

Available online 12 November 2022

Keywords:

High-entropy alloy

Heterogeneous structure

Strength and ductility

Hetero-deformation induced hardening

Strain hardening

ABSTRACT

Alloys with high yield strength and ductility are attractive for application because of their potential to offer mass reduction, energy savings, and enhanced structural reliability. However, increasing strength usually comes at the expense of ductility, which is commonly known as the strength-ductility trade-off for metal alloys. In this work, we explored a strategy of using a heterogeneous grain size structure and a reduced stacking fault energy in a CoCrFeNiMn FCC high entropy alloy to overcome the limitations of this trade-off. By this approach, the alloy achieved a yield strength of 980 MPa, a tensile strength of 1385 MPa, and tensile elongation to failure of 48% benefiting from cooperative strain hardening via multiple mechanisms, such as hetero-deformation induced (HDI) hardening, deformation twinning, Frank-Read dislocation sources and Lomer-Cottrell dislocation locks instigated by such structures. These micromechanisms of deformation help to harden the alloy via in situ refinement of the mean free paths for dislocations.

© 2022 Acta Materialia Inc. Published by Elsevier Ltd. All rights reserved.

1. Introduction

High-entropy alloys (HEAs) are a class of metal alloys characterized by a high number of principal elements in roughly equal molar proportions in their compositions. Conventionally, the minimum number of elements has been defined as five. Since the discovery of the concept in CuCoNiCrAl_xFe [1] and FeCrMnNiCo [2] alloys, many new alloy systems have been invented in the past two decades. The increasingly diverse alloy systems provide a wide space for microstructure and property designs. As a result, many HEAs have been developed with superior mechanical properties in comparison to traditional alloys, such as high ultimate strength, high fracture toughness, high fatigue resistance,

high elastic strain limit (~2%), unique Elinvar effect and high mechanical performance at elevated temperatures [3–5].

Most HEAs are found in two main types of crystal structures, i.e., body-centered cubic (BCC) and face-centered cubic (FCC) structures. Generally, single-phase FCC structured HEAs are based on 3d transition elements. They tend to exhibit high tensile ductility and fracture toughness at room temperature due to their FCC crystal structure with more slip systems, such as CrCoFeNi-based alloys [6–15]. By the same token, they have relatively low yield strengths (<1 GPa) [16,17]. To increase the yield strength of FCC HEAs, severe plastic deformation and grain size refinement strategies have been applied [18–20]. However, a common challenge remains as to conventional alloys: as strength increases, ductility decreases [21]. This is because the strain hardening rate ($\dot{\theta}$) can no longer keep up with the continuously increasing flow stress ($\dot{\theta} < \dot{\sigma}$). This leads to unstable plastic deformation, i.e., necking, according to the Considère criterion [18]. Thus, the main approach to suppressing such deformation instability is to maintain a high $\dot{\theta}$ at high stress levels.

* Corresponding authors.

E-mail addresses: scmao@bjut.edu.cn (S. Mao), yinong.liu@uwa.edu.au (Y. Liu), xdhan@bjut.edu.cn (X. Han).

One approach to achieving a high strain hardening rate has been to lower the stacking fault energy to encourage deformation twin-induced plasticity [6]. Twin boundaries are known to be the sources of glissile partial dislocations and at the same time restrict dislocation movement to enhance strain hardening [6,10,22]. However, this strategy is usually effective in coarse-grained alloys at low yield strengths; therefore, the yield strength is still low.

Creating heterogeneous structures has proven to be another effective way to overcome the strength-ductility trade-off [23,24]. In such structures, geometrically necessary dislocations pile up at hetero-interfaces due to deformation incompatibility between these heterogeneous components. This leads to strain hardening known as hetero-deformation induced (HDI) hardening [25]. Generally, more complex heterostructures involving multiscale (e.g., gradient, bimodal, lamellar, etc., configurations) and multiple components (e.g., grains and phases) are more effective for HDI hardening [26–29]. For example, a gradient dislocation cell structure in an Al_{0.1}CoCrFeNi HEA created by cyclic torsion is able to increase its yield strength by 100% to 550 MPa with only a 30% sacrifice of its uniform ductility [23]. Another Al_{0.1}CoCrFeNi HEA sample gained a 144% increase in the yield strength at a 29% loss of ductility after cold rolling and annealing treatment [30]. These studies have substantially advanced the current benchmark for strength-ductility dual enhancement.

In this study, we explored a new approach to further enhance the strength without compromising the ductility in a single-phase FCC HEA. The idea is to create a bimodal grain heterostructure for HDI hardening to enhance the strength and by careful composition design to lower the SFE to encourage the formation and activities of deformation twins for better ductility. Such microstructures are rarely deployed in HEAs, and the corresponding strain hardening mechanism for HEAs with such heterostructure structures and low stacking fault energy has not been explored. Thus, the findings of this study may reveal useful information for designing high-performance HEAs.

2. Experiment

2.1. Design of chemical composition

The alloy system chosen for this study was the equiatomic Co₂₀Cr₂₀Fe₂₀Mn₂₀Ni₂₀ FCC high-entropy alloy. It has been the focus of many studies in the past two decades due to its high ductility and fracture toughness at room temperature and even 77 K [8,10–12,31,32]. In this work, we aim to lower its stacking fault energy of 25 mJ/m² [33] to promote deformation twinning for better strain hardening and ductility [16].

In this system, Ni has the highest stacking fault energy (125 mJ/m²), and Co has the lowest stacking fault energy (−1 mJ/m²) at room temperature [34,35]. Cr, Fe and Mn have medium stacking fault energy [33]. Therefore, the Ni content was reduced, and the Co and Cr contents were increased to a nonequiatomic Co₃₀Cr₂₀Fe₁₈Ni₁₄Mn₁₈ composition. As a result, the stacking fault energy of the alloy is reduced to 16.3 mJ/m².

Five thermodynamic parameters are used as empirical criteria to assure a single-phase FCC structure for the alloy: enthalpy of mixing (ΔH_{mix}), entropy of mixing (ΔS_{mix}), Ω (defined as $\frac{T_m \Delta S_{mix}}{|\Delta H_{mix}|}$), atomic size difference (δ), and valence electron concentration (VEC). These parameters can be calculated by Eqs. (1–3) [36]:

$$\left\{ \begin{array}{l} \Omega = \frac{T_m \Delta S_{mix}}{|\Delta H_{mix}|} \\ \Delta H_{mix} = 4 \sum_{i < j} c_i c_j \Delta H_{ij} \\ \Delta S_{mix} = -R \sum_{i=1}^n c_i \ln c_i \end{array} \right. \quad (1)$$

$$\left\{ \begin{array}{l} \delta_r = \sqrt{\sum_{i=1}^n c_i (1 - \frac{r_i}{\bar{r}})^2} \\ \bar{r} = \sum_{i=1}^n c_i r_i \end{array} \right. \quad (2)$$

$$VEC = \sum_{i=1}^n c_i (VEC)_i \quad (3)$$

where c_i and c_j are the mole fractions of elements i and j , ΔH_{ij} is the enthalpy of mixing between elements i and j , R is the gas content (8.314 J/(mol·K)), T_m is the melting temperature of the alloy ($T_m = 1307$ °C), which can be determined by thermodynamic calculation using JMatPro software, r_i is the atomic radius of element i , \bar{r} is the weighted average radius of the elements, and $(VEC)_i$ is the valence electron concentration of element i . The atomic radii and valence electron concentrations of the constituent elements of the alloy can be seen in Table S1 (Supplementary Information). Table S2 shows the enthalpy of mixing of the element pairs. For the Co₃₀Cr₂₀Fe₁₈Ni₁₄Mn₁₈ alloy, the five parameters calculated are $\Delta S_{mix} = 13.13$ J/(k·mol), $\Delta H_{mix} = -3.9$ kJ/mol, $\Omega = 5.51$, $\delta = 0.39\%$, and $VEC = 8.0$. All parameters are well within acceptable values for maintaining an FCC single-phase structure, which are 11–19.5 J/(k·mol) for ΔS_{mix} , −15–5 kJ/mol for ΔH_{mix} , >1.1 for Ω , <6.6% for δ , and >8.0 for VEC [37–39].

The phase diagram of the Co₃₀Cr₂₀Fe₁₈Ni₁₄Mn₁₈ alloy was calculated using JMatPro software [40] and is shown in Fig. S1. The alloy is in the FCC phase above 522 °C, below which the alloy partially transforms to BCC. It is known that the FCC → BCC transformation in this work is suppressed when $(T_S - T_T)/T_S > 0.3$, where T_S is the solidus temperature and T_T is the phase transformation temperature [41,42]. For the Co₃₀Cr₂₀Fe₁₈Ni₁₄Mn₁₈ alloy, $T_T = 522$ °C and $T_S = 1275$ °C; thus, $(T_S - T_T)/T_S = 0.59$. This implies that the FCC → BCC transformation predicted by thermodynamic calculation is prohibited in practice and that the alloy remains in FCC at room temperature.

2.2. Alloy preparation

The Co₃₀Cr₂₀Fe₁₈Ni₁₄Mn₁₈ alloy was prepared by vacuum suspension melting in an argon atmosphere using high-purity metals Co, Cr, Fe, Ni and Mn (>99.9 wt%). A 3 kg ingot (φ60 mm × 130 mm) was repeatedly melted seven times to eliminate compositional segregation (Fig. S2). The cast alloy was homogenized at 1200 °C for 24 h. The homogenized alloy was then cold rolled to plate form and annealed at 900 °C for 5 h. After that, the plate was cold rolled again to a thickness reduction of ~80% to 1.2 mm, annealed at 730, 780 and 820 °C for 10 min and then water quenched. The plate samples were designated RA-730, RA-780 and RA-820, respectively. Fig. S3 illustrates the thermomechanical processing of the alloy.

2.3. Microstructure and phase identification

The crystal structures of the samples were investigated by means of X-ray diffraction (XRD) with Cu-Kα radiation. The microstructures of the alloys were examined using an optical microscope and an FEI Quanta 650F scanning electron microscope (SEM). The SEM is equipped with energy-dispersive X-ray spectroscopy (EDS) for chemical analysis and an electron backscatter diffraction (EBSD) detector for crystallographic analysis. EBSD samples were fabricated by mechanical polishing followed by electropolishing in an aqueous solution of HClO₄:C₂H₅OH = 1:10 by volume at 20 V and −20 °C. An aberration-corrected FEI Titan Themis G2-300 kV transmission electron microscope (TEM) was

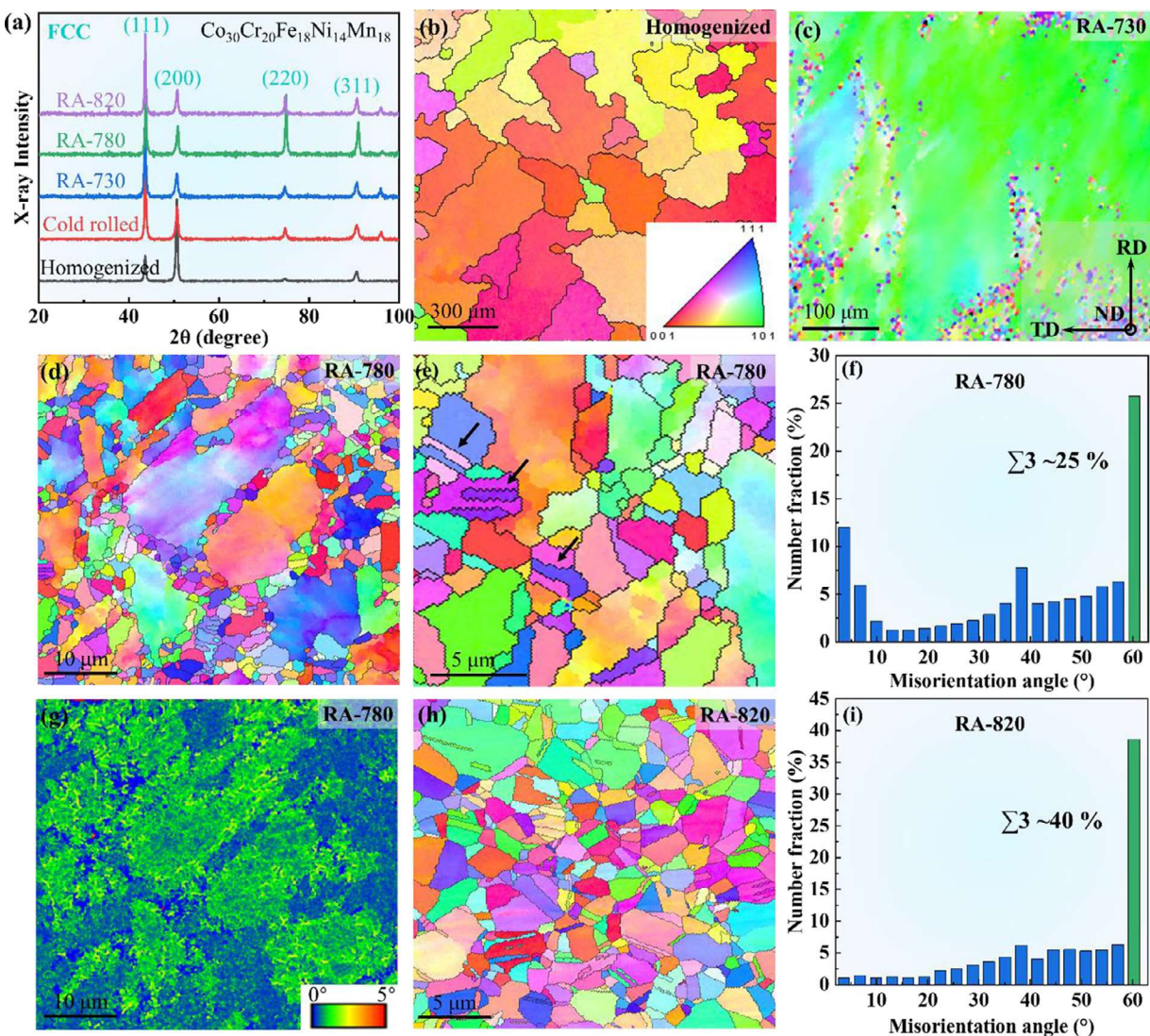


Fig. 1. Microstructures of the $\text{Co}_{30}\text{Cr}_{20}\text{Fe}_{18}\text{Ni}_{14}\text{Mn}_{18}$ HEA after different treatments. (a) XRD patterns of the alloy under different treatment conditions, including the homogenized, cold-rolled and annealed. (b) Microstructure of the homogenized sample presented as an EBSD orientation map. The inset is an inverse pole figure map to show the color correspondence to the crystallographic orientations. (c) Microstructure of the RA-730 sample. (d) Microstructure of the RA-780 sample. (e) Microstructure of the RA-780 sample at a higher magnification to reveal the annealing twins. (f) The distribution of grain misorientation angles corresponding to (d). (g) Kernel average misorientation map corresponding to (d). (h) Microstructure of the RA-820 sample. (i) The distribution of grain misorientation angles corresponding to (h).

used to analyze the microstructure and elemental distributions at the nano- and atomic levels. The TEM samples were first mechanically ground to a thickness of $30 \mu\text{m}$ and then electrolytically jet polished in an $\text{HClO}_4:\text{C}_2\text{H}_5\text{OH} = 1:10$ electrolyte. The in situ deformation of the sample was performed using an in situ tensile TEM sample holder (Bestron-INSTEMS-M). The in situ TEM test sample was micromachined using a focused ion beam (FIB, FEI-Helios-NanoLab-600i).

2.4. Mechanical properties

An Instron 5966 tensile tester was used to characterize the tensile mechanical properties of the alloys. Dog bone-shaped samples with a gauge section of $15 \times 2.5 \times 1.2 \text{ mm}$ were cut from the plates. A constant strain rate of $1 \times 10^{-3} \text{ s}^{-1}$ was used. The digital image correlation (DIC) method with the LaVision-DaVis data acquisition package was used to study the strain field upon tensile deformation.

3. Results

3.1. Microstructure

Fig. 1 shows a microstructural analysis of the $\text{Co}_{30}\text{Cr}_{20}\text{Fe}_{18}\text{Ni}_{14}\text{Mn}_{18}$ alloy. Fig. 1(a) shows XRD patterns of five samples, including the homogenized, cold-rolled, and the three annealed samples. All five patterns are indexed to the same single-phase FCC structure with a lattice parameter of 0.358 nm . Chemical analysis, as summarized in Table S3 (more information is presented in Figs. S4 and S5), indicated a uniform distribution of all elements and a composition close to the nominal. Fig. 1(b) shows the microstructure of the alloy after the homogenization treatment as an inverse pole figure crystal orientation map. The color code for the crystallographic directions is indicated in the inset. The homogenized sample had large grains with an average size of $300 \mu\text{m}$. Fig. 1(c) shows the microstructure of the RA-730 sample. It is apparent that the sample had not recrystallized and that it had a

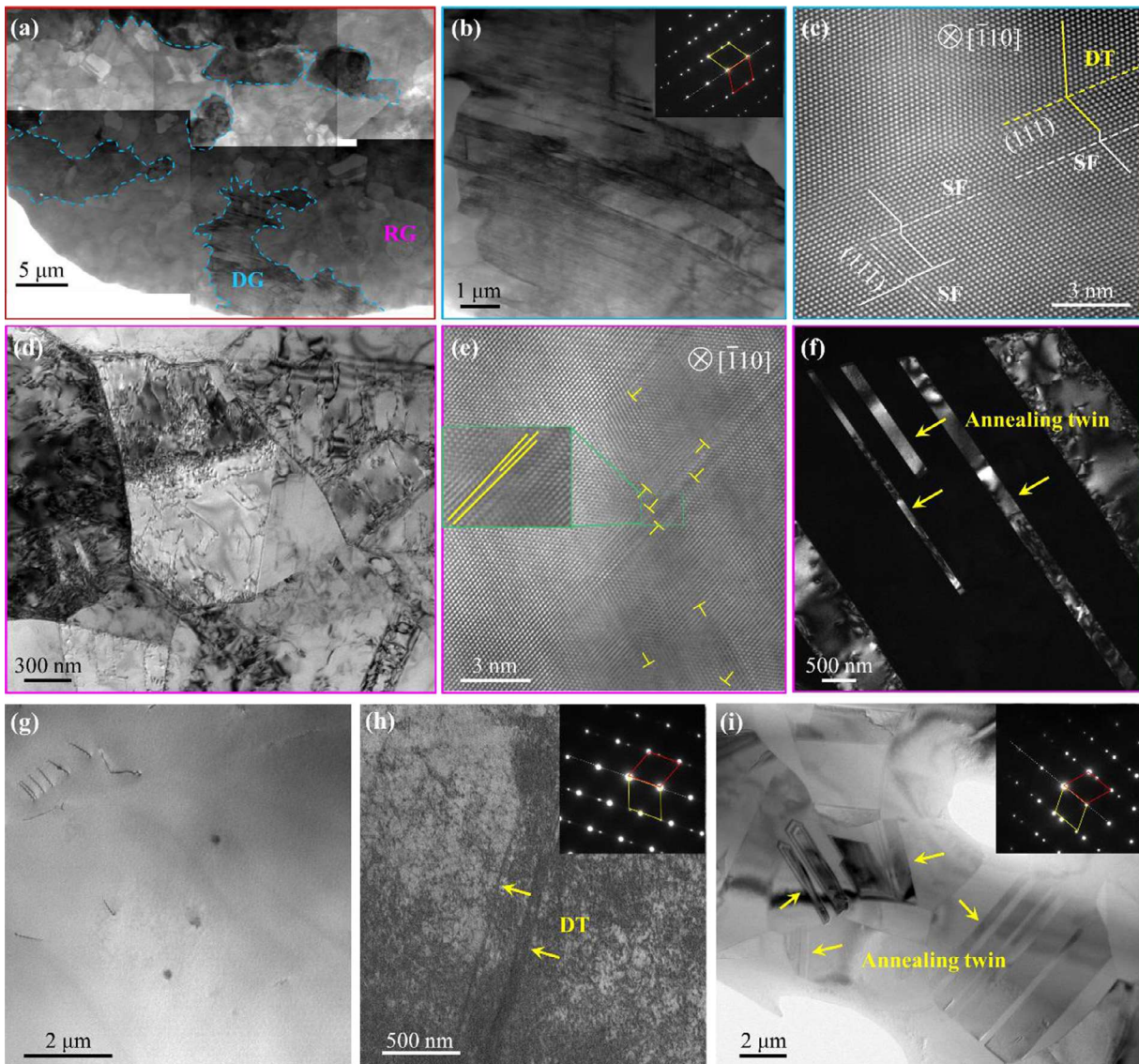


Fig. 2. Microstructures of the $\text{Co}_{30}\text{Cr}_{20}\text{Fe}_{18}\text{Ni}_{14}\text{Mn}_{18}$ alloy after different treatments. (a) BF-STEM image of the RA-780 sample. (b) BF-STEM image of the deformed grain at a higher magnification to reveal the deformation twins. The inset shows an SAED. It is indexed to $(111)[\bar{1}1\bar{2}]$ in the $[\bar{1}10]$ zone axis. (c) A high-resolution HAADF-STEM image of a deformed grain showing deformation twins (DT) and stacking faults (SF). (d) TEM image of the small recrystallized grains. (e) HRTEM image of the interior of a recrystallized grain. The inset is the magnified image showing a dislocation. (f) DF-TEM image of a recrystallized grain showing annealing twins. (g) TEM image of the homogenized sample. (h) TEM image of the RA-730 sample. The inset is the SAED at the $[\bar{1}10]$ zone axis, showing the deformation twin structure. (i) TEM image of the RA-820 sample. The inset is the SAED at the $[\bar{1}10]$ zone axis, showing the annealing twin structure.

dominant $\langle 110 \rangle$ preferential orientation in the plate normal direction. Fig. 1(d) shows the microstructure of the RA-780 sample. The sample was obviously recrystallized with two distinctive populations of grains of different sizes, with an average size of $\sim 1 \mu\text{m}$ for the smaller grains and $\sim 18 \mu\text{m}$ for the large grains. Fig. 1(e) shows the small grains in the sample at a higher magnification. Some twins are apparent (indicated by the black arrows). Fig. 1(f) shows the grain misorientation angle distribution of the sample. It is apparent that there is a high population of grains with a misorientation of 60° . They are annealing twins ($\sum 3$). It is clear that the number fraction of annealing twins is 25%. Fig. 1(g) is a kernel average misorientation map of the RA-780 sample. The large grains appear to have relatively larger kernel average misorientation angles of $<3^\circ$ than the smaller grains at $<1^\circ$. The kernel average misorientation angle measures for the local lattice tilt, e.g., caused by a dislocation defect, and thus is considered related to the dislocation density [43]. This observation suggests a higher dislocation

density in the larger grains than in the smaller grains. Thus, the smaller grains are considered to be recrystallized grains, and larger grains are considered to be deformed grains. Fig. 1(h) shows the microstructure of the RA-820 sample. The sample is fully recrystallized with equiaxial grains of about $8 \mu\text{m}$ in average size. Some annealing twins are also obvious. Fig. 1(i) shows the grain misorientation angle distribution of the sample. The number population of annealing twins is $\sim 40\%$.

Fig. 2 shows a TEM analysis of the microstructures of the $\text{Co}_{30}\text{Cr}_{20}\text{Fe}_{18}\text{Ni}_{14}\text{Mn}_{18}$ alloy. Fig. 2(a) shows a series of bright-field scanning transmission electron microscopy (BF-STEM) images of the RA-780 sample. The sample contained small recrystallized grains (RG) and large deformed grains (DG). Fig. 2(b) shows a deformed grain at a higher magnification. The grain contained a high density of dislocations. The inset shows a selected area electron diffraction (SAED) pattern. The pattern is indexed to a $(111)[\bar{1}1\bar{2}]$ twin in the $[\bar{1}10]$ zone axis. These are deformation twins. They

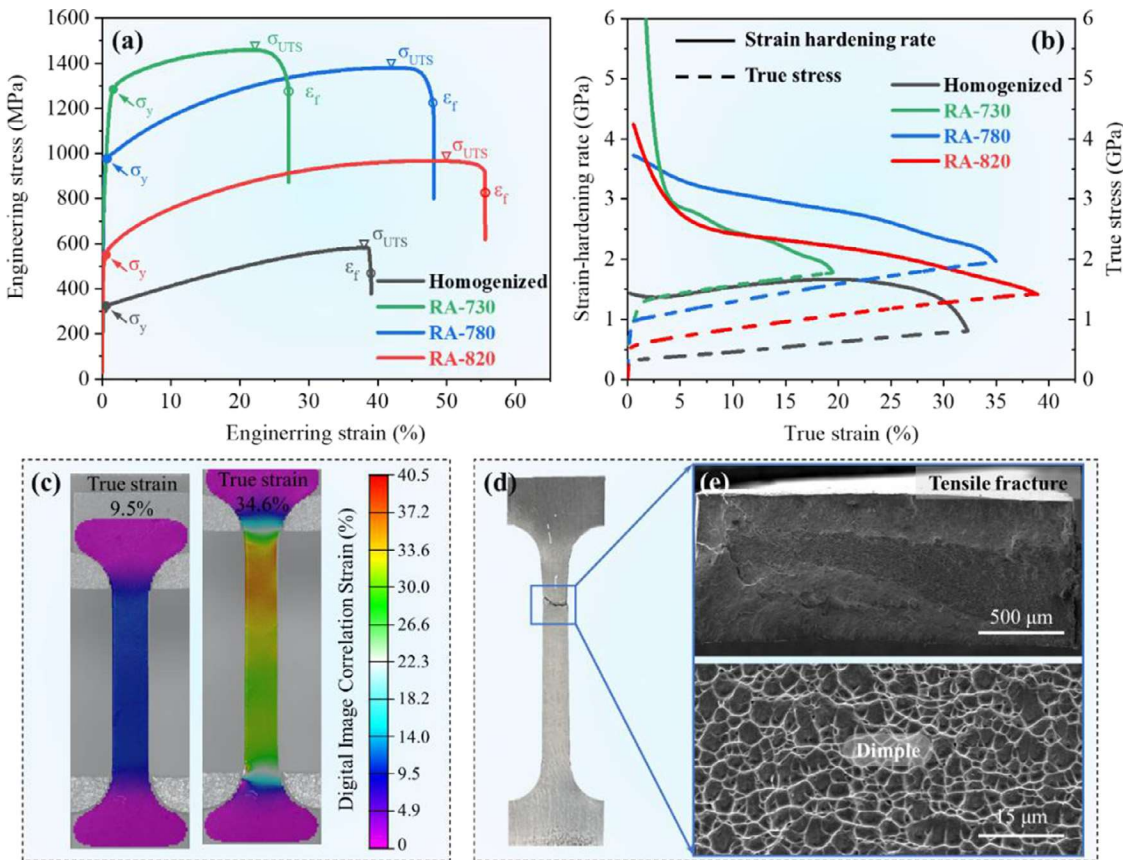


Fig. 3. Mechanical properties of $\text{Co}_{30}\text{Cr}_{20}\text{Fe}_{18}\text{Ni}_{14}\text{Mn}_{18}$ alloy in different heat treatment states. (a) Tensile engineering stress–strain curves of the homogenized and three annealed samples. (b) Corresponding true stress–strain curves and the strain-hardening rate curves of the four samples. (c) Von Mises strain map images of the RA-780 sample at 9.5% and 34.6% true strains, showing uniform deformation. (d) Optical image of the RA-780 sample after tensile rupture, showing no sign of macroscopic necking. (e) SEM image of the ruptured surface of the RA-780 sample, showing a typical dimpled ductile rupture morphology.

are generally thin plates of approximately ten nanometers in thickness and are difficult to reveal using the EBSD method; therefore, only annealing twins can be seen in Fig. 1(d). Fig. 2(c) shows an atomic resolution high-angle annular dark field (HAADF)-STEM image from the grain. A few stacking faults are present. Fig. 2(d) shows a recrystallized grain, and Fig. 2(e) shows a high-resolution image of the grain. The grain contained some partial dislocations. Fig. 2(f) shows a dark-field (DF)-TEM image of recrystallized grains. The annealing twins are several micrometers in thickness, distinctive from the much thinner deformation twin plates seen in Fig. 2(b).

Fig. 2(g) shows a TEM image of the homogenized sample. Only some intrinsic dislocations were observed in the large grain. Fig. 2(h) shows a TEM image of the RA-730 sample. The inset is an SAED pattern, revealing a deformation twin structure. Thus, a high density of dislocations and deformation twins were formed in the cold worked grains. Fig. 2(i) shows a TEM image of the RA-820 sample. The sample was fully recrystallized, and the grains contained a high density of annealing twins, as indicated by the yellow arrows. The inset shows an SAED pattern of the area, revealing the twinned structure. No dislocations and deformation twins were observed.

These observations demonstrate that the RA-780 sample was partially recrystallized and had a heterogeneous structure at two levels: microscale grain structure heterogeneity and nanoscale defect heterogeneity of dislocations, stacking faults, deformed twins and annealing twins. RA-730 and RA-820 samples, on the other hand, showed insignificant microstructural heterogeneity. The RA-

730 sample showed cold worked grains with dislocations and deformation twins, and the RA-820 sample showed fully recrystallized grains with annealing twins, revealing nanoscale heterogeneity but without microscopic heterogeneity.

3.2. Tensile properties and strain-hardening behavior

Fig. 3 presents mechanical testing and analysis of the $\text{Co}_{30}\text{Cr}_{20}\text{Fe}_{18}\text{Ni}_{14}\text{Mn}_{18}$ alloy. Fig. 3(a) shows the tensile engineering stress–strain curves of four samples after different heat treatments. The RA-730 sample showed the highest yield strength ($\sigma_y = 1300 \text{ MPa}$), and the RA-820 sample showed the highest tensile elongation to failure ($\varepsilon_f = 56\%$), but the RA-780 sample showed the best combination of strength and ductility, with a yield strength of 980 MPa and a ductility of 48% tensile elongation to failure. The RA-780 sample also exhibited the highest strain hardening effect among all the samples, with a strength increase of 405 MPa from the yield strength to reach an ultimate tensile strength of 1385 MPa.

A high strain hardening rate ($\theta = \frac{d\sigma_{true}}{d\varepsilon_{true}}$) is considered a primary reason for preventing necking to reach high strength and ductility [44]. Fig. 3(b) shows the true stress–true strain curves (the dashed curves) and the strain hardening rate versus true strain curves (the solid curves) for the four samples. It is seen that the RA-780 sample exhibited the highest strain hardening rate among all samples during the plastic yielding stage. It is also noted that for the RA-780 sample, $\theta > \sigma_{true}$ till 35% true strain. Fig. 3(c) shows DIC images of the von Mises strain maps of the RA-780

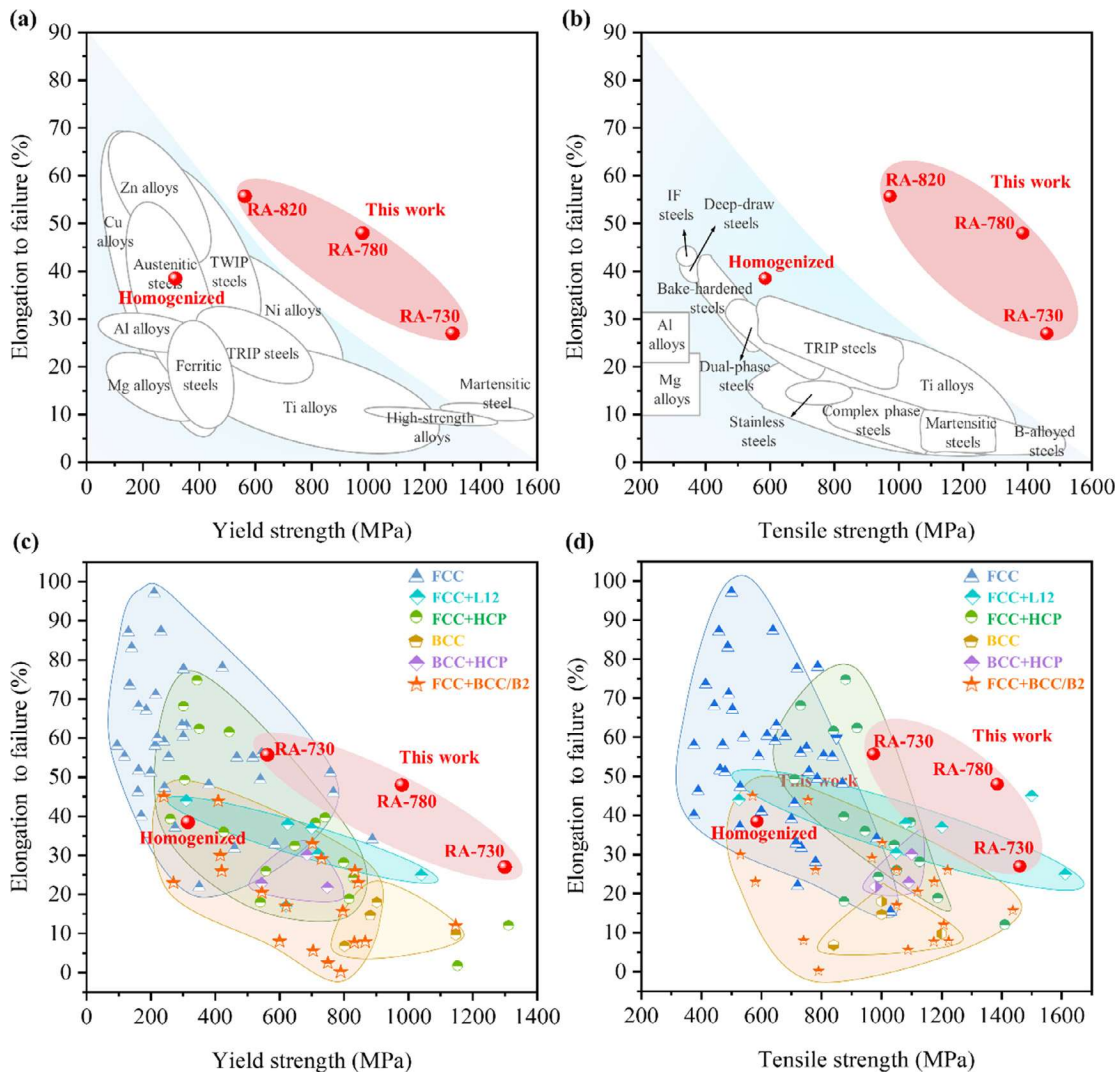


Fig. 4. Comparison of the tensile properties of the $\text{Co}_{30}\text{Cr}_{20}\text{Fe}_{18}\text{Ni}_{14}\text{Mn}_{18}$ alloy and other engineering alloys. (a) Comparison of the yield strength and tensile elongation to failure between the $\text{Co}_{30}\text{Cr}_{20}\text{Fe}_{18}\text{Ni}_{14}\text{Mn}_{18}$ alloy samples and common engineering alloys. (b) Comparison of the ultimate tensile strength and tensile elongation to failure between the $\text{Co}_{30}\text{Cr}_{20}\text{Fe}_{18}\text{Ni}_{14}\text{Mn}_{18}$ alloy samples and common engineering alloys. (c) Comparison of the yield strength and tensile elongation to failure between the $\text{Co}_{30}\text{Cr}_{20}\text{Fe}_{18}\text{Ni}_{14}\text{Mn}_{18}$ alloy samples and common high entropy alloys reported in the literature. (d) Comparison of the ultimate tensile strength and tensile elongation to failure between the $\text{Co}_{30}\text{Cr}_{20}\text{Fe}_{18}\text{Ni}_{14}\text{Mn}_{18}$ alloy samples and common high entropy alloys reported in the literature.

sample at two different stages during the deformation process. It is evident that the deformation was uniform within the gauge length. Fig. 3(d) shows an optical image of the ruptured RA-780 sample. It is evident that the sample experienced no necking till rupture. Fig. 3(e) displays two SEM images of the ruptured surface, revealing a typical dimpled morphology of plastic rupture.

Fig. 4 shows a comparison of the tensile properties (σ_y , σ_{UTS} and ε_f) between $\text{Co}_{30}\text{Cr}_{20}\text{Fe}_{18}\text{Ni}_{14}\text{Mn}_{18}$ alloy samples and other alloys. Figs. 4(a) and (b) show the comparison with some common engineering alloys. It is apparent that whereas the homogenized sample appeared to be comparable to the common engineering alloys, the heat-treated samples are clearly more superior in combined strength and ductility to all the comparison alloys, including TWIP/TRIP steels [45]. Figs. 4(c) and (d) show the comparison with other single-phase and dual-phase HEAs reported in the literature [17,46–52] (Supplementary Table S4 for detailed information). The homogenized sample may be considered of low performance relative to these comparison alloys, but the heat-treated samples, particularly the RA-780 sample, appear to outperform all the comparison alloys, including the ultrastrong and ductile coherent/incoherent L₁/₂/B₂ precipitation-reinforced HEA, such

as $(\text{CoCrFeNi})_{94}\text{Ti}_2\text{Al}_4$ [53], $\text{Al}_{0.7}\text{Fe}_2\text{Mn}_{1.8}\text{Ni}$ [54] and $\text{AlCrFe}_2\text{Ni}_2$ [55] HEAs.

3.3. Hetero-deformation induced hardening

It is generally known that the strain hardening rate increases with increasing average grain size for alloys with homogeneous microstructures. Large grains offer more space for dislocation storage, thus enabling higher dislocation densities and more intense interactions between them [56,57]. It is also known that heterogeneous microstructures may further increase the strain hardening rate [24,27,58], as seen for the RA-780 sample in Fig. 3(b). Heterogeneous microstructures cause geometrically necessary dislocation pile-ups at the hetero-interfaces, due to the deformation incompatibility between the “soft” and “hard” regions, creating long-range back stress in a soft region and forward stress in a hard region. The development of back stress and forward stress during the hetero-deformation increase the resistance to plastic deformation, resulting in strengthening and extra work hardening of materials. This is known as hetero-deformation induced (HDI) hardening [25].

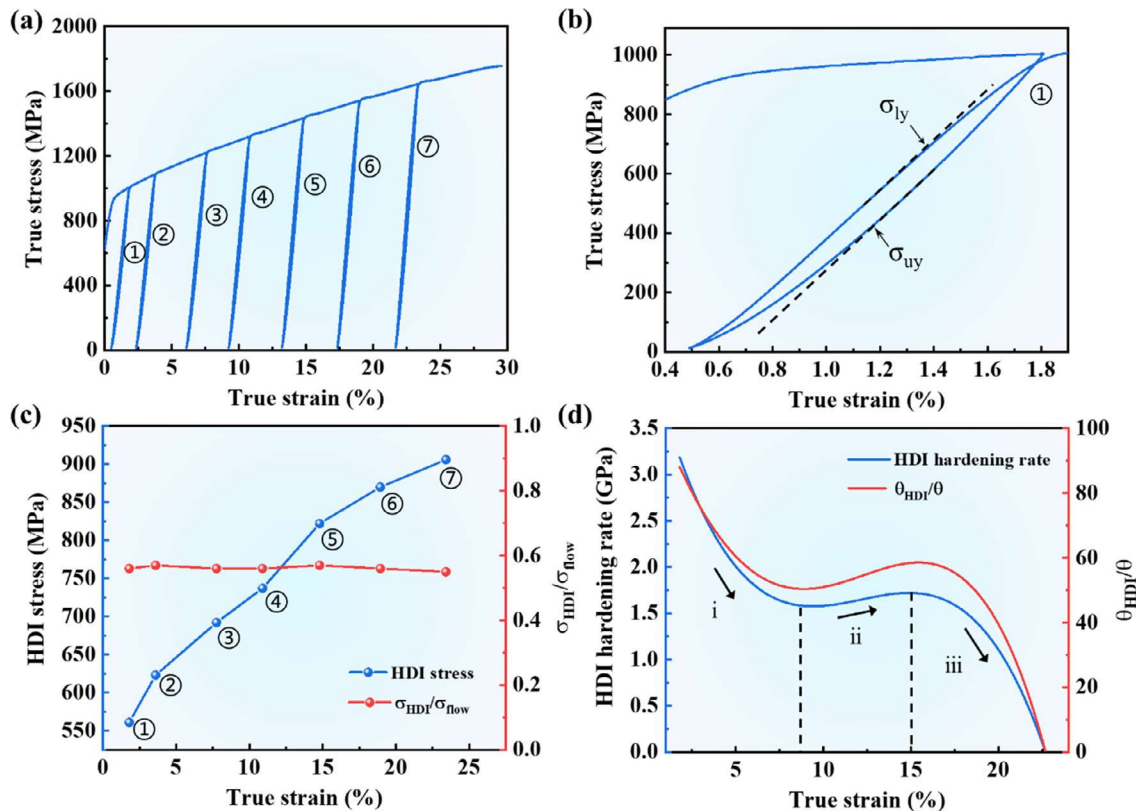


Fig. 5. HDI hardening of the RA-780 sample. (a) Loading–unloading–reloading stress–strain curves of the RA-780 sample. (b) The hysteresis loop of the first unloading–reloading curve. (c) HDI stress and $\sigma_{\text{HDI}}/\sigma_{\text{flow}}$ versus true strain curves of the RA-780 sample. (d) HDI hardening rate and $\theta_{\text{HDI}}/\theta$ versus true strain curves of the RA-780 sample.

The HDI stress can be evaluated by analyzing the loading–unloading hysteresis loops, which were equal to the “back stress” measured from the loading–unloading–reloading test method [25,59,60]. Fig. 5(a) shows a loading–unloading–reloading test of the RA-780 sample. Fig. 5(b) displays the first unloading–reloading hysteresis loop. In this figure, the yielding stress upon loading (σ_{ly}) and that upon unloading (σ_{uy}) can be determined. The HDI stress can then be computed as $\sigma_{\text{HDI}} = (\sigma_{\text{ly}} + \sigma_{\text{uy}})/2$ [30,58]. Fig. 5(c) plots the HDI stress versus true strain for the RA-780 sample. At the near yielding point of $\varepsilon_{\text{true}} = 1.8\%$, the HDI stress is measured at 561 MPa, which is approximately 56% of the yield strength, indicating that the high yield strength of the RA-780 sample mainly resulted from the high HDI stress. It is also clear that the HDI stress increased with increasing deformation, reaching a maximum value of 906 MPa at $\varepsilon_{\text{true}} = 23.4\%$, which was even higher than the ultimate tensile strength of the RA-820 sample and other heterogeneous structured alloys [30,34,61,62]. Additionally, plotted in the figure is $\sigma_{\text{HDI}}/\sigma_{\text{flow}}$. The $\sigma_{\text{HDI}}/\sigma_{\text{flow}}$ ratio remained unaffected by the level of deformation. The trends of both σ_{HDI} and $\sigma_{\text{HDI}}/\sigma_{\text{flow}}$ reveal the crucial role of HDI strengthening throughout tensile deformation.

Fig. 5(d) shows the HDI hardening rate (θ_{HDI}) of the RA-780 sample, which is computed from the HDI stress–strain curves as $\theta_{\text{HDI}} = \frac{d\sigma_{\text{HDI}}}{d\varepsilon}$ (Fig. 5(c)). The θ_{HDI} curve shows three stages, with a decreasing, increasing and then decreasing trend. Such behavior is unexpected and is in contrast to the $\text{Al}_{0.1}\text{CoCrFeNi}$ and $\text{Co}_{34.46}\text{Cr}_{32.12}\text{Ni}_{27.42}\text{Al}_3\text{Ti}_3$ heterogeneous structured alloy [30,60]. The increase in θ_{HDI} in stage (ii) implies triggering other deformation mechanisms, leading to the introduction of an extra HDI hardening mechanism during plastic deformation. The figure also displays a $\theta_{\text{HDI}}/\theta$ curve, which follows a similar trend to the θ_{HDI}

curve. The decreases in $\theta_{\text{HDI}}/\theta$ in stages (i) and (iii) imply the occurrence of other strain hardening mechanisms, which play a particularly important role, especially in stage (iii) [60].

3.4. Ex situ micromechanisms of deformation in heterostructured RA-780

Fig. 6 shows a TEM analysis of the microstructure of deformed grains in the RA-780 sample after deforming to 2% strain. Fig. 6(a) is a HAADF-STEM image taken in a recrystallized grain. The recrystallized grains contained a low density of dislocations (white arrows) and some nanosized deformation twins (yellow arrows), revealing a dual deformation mechanism at low strains. Fig. 6(b) shows a TEM image of a recrystallized grain and a deformed grain. A significant accumulation of dislocations can be seen in the recrystallized grain close to the boundary with the deformed grain. Fig. 6(c) shows a TEM image of an annealing twin in a recrystallized grain. Similarly, at the twin boundary, long-range columns of dislocations accumulate, indicating the effect of hetero-interfaces as obstacles for dislocation movement. These long-range columns of dislocations, in conjunction with the annealing twins, form ‘cages’ (~800 nm in diameter) that constrain dislocation movement within, as indicated by the white arrows. These ‘cages’ may provide further hardening.

Fig. 6(d) shows a HAADF-STEM image of a deformed grain. It contained a high density of deformation twins and dislocations. The SAED pattern shown in the inset reveals a $(1\bar{1}1)[1\bar{1}2]$ deformation twin structure. Fig. 6(e) shows a DF-TEM image of deformed grain at a higher magnification. The deformation twin plates are about 9 nm thick. Fig. 6(f) shows a BF-TEM image of the interior of the grain, showing that the deformed grain contained a

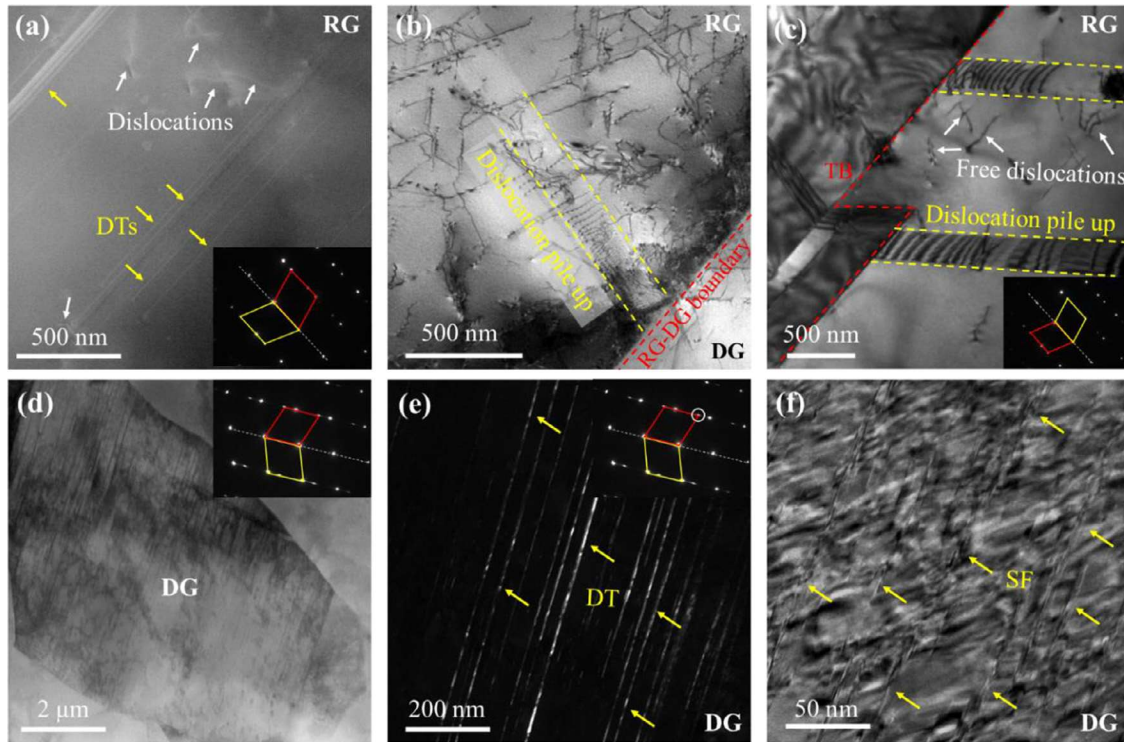


Fig. 6. TEM analysis of the microscopic mechanisms of deformation of the RA-780 sample at 2% tensile strain. (a) HAADF-STEM image of a recrystallized grain, which contains dislocations and deformation twins. The inset shows an SAED pattern of the annealing twins in the [011] zone axis. (b) TEM image of a recrystallized grain and a deformed grain, revealing dislocation pile-ups at the boundary. (c) TEM image of a recrystallized grain region, showing dislocation pile-ups at the boundary of an annealing twin. The inset shows an SAED pattern of the annealing twins in the [011] zone axis. (d) Microstructure of a deformed grain showing a high density of defects. The inset shows an SAED pattern of annealing twins in the [011] zone axis. (e) DF-TEM image of the interior of the deformed grain seen in (d), displaying a high density of deformation twins. (f) BF-TEM image of the interior of the deformed grain at a higher magnification, showing a high density of stacking faults.

significant number of stacking faults. The densities of deformation twins, stacking faults and dislocations in the deformed grains at 2% strain are similar to those in the cold rolled grains prior to tensile deformation (Figs. 2(a)-(c)).

Fig. 7 shows a TEM analysis of the microstructure of recrystallized grains in the RA-780 sample after deformation to 10% strain. Fig. 7(a) shows a STEM image of one recrystallized grain. The microstructure contained a high density of stacking faults on different {111} planes. Fig. 7(b) shows a HAADF-STEM image of the stacking faults. The stacking faults form into in situ network cells of ~50 nm across, much smaller than the average spacing (~800 nm) between the long-range columns of dislocations. Fig. 7(c) shows a high-resolution HAADF-STEM image of the stacking faults stemming from adjacent {111} planes, forming Lomer-Cottrell (L-C) locks. Fig. 7(d) shows the HAADF-STEM image of the Lomer-Cottrell and dislocation structures. It is clear that the blocked dislocation is a 1/2[110] 60° full dislocation consisting of two partial dislocations and a stacking fault in between ($\frac{1}{2}<110>\rightarrow\frac{1}{6}<1\bar{1}\bar{2}>+\text{SF}+\frac{1}{3}<121>$). Fig. 7(e) shows the lattice strain of the HAADF-STEM image, which is calculated in the horizontal directions using the peak pairs algorithm [63]. The obvious distribution of extension (pink) and compression (red) strain regions implies lattice differences. Fig. 7(f) shows the overlapping ε_{xx} strain maps with the corresponding HAADF-STEM images. It is noted that the highest stress field localized around the Lomer-Cottrell lock, which is responsible for providing high lattice frictional stress for pinning dislocations [64].

Fig. 8 shows a TEM analysis of the microstructure of recrystallized grains in the RA-780 sample after deformation to 25% and 40% strains. Fig. 8(a) shows a HAADF-STEM image of the interior of a recrystallized grain in a sample deformed to 25% strain. A high

density of nanosized deformation twins have been formed. The average twin thickness is ~8 nm, and the average spacing is ~25 nm. These values are larger than the critical space (~6 nm) for the activation of partial dislocations and facilitating those dislocations gliding on the plane that intersect with twin boundaries, resulting in a dynamic strain strengthening effect [65]. Fig. 8(b) presents a high-resolution HAADF-STEM image of deformation twins. It is clear that the partial dislocation was inspired and glide from one side of the twin boundary to the other, forming a cross stacking fault, indicating that the twin boundary can obstruct the motion of dislocations. Fig. 8(c) shows a high-resolution HAADF-STEM image for the twin boundary. This reveals that the partial dislocations emission from the twin boundary and slip to the matrix, forming stacking faults in the matrix. Thus, the mean free path of dislocations, as defined by the average spacing between the deformation twin and matrix, was ~16.5 nm.

Fig. 8(d) is a STEM image of a recrystallized grain in a sample deformed to 40% strain. The inset is a DF-TEM image corresponding to Fig. 8(d). After such high plastic deformation, some secondary deformation twins were formed in both the matrix and the primary deformation twins. The secondary twins are much thinner and are inclined at 70.5° to the primary deformation twin boundaries. Fig. 8(e) shows the atomic structure of a secondary deformation twin. The spacing and the thickness are both approximately 8 nm. Fig. 8(f) displays a HAADF-STEM image of a region containing secondary deformation twins and stacking faults. The twin boundaries are indicated by the white dotted lines, and the stacking faults are indicated by the yellow dotted lines. These two structures interact and form a typical tight network structure of ~5 nm. This further reduces the mean free path for dislocations.

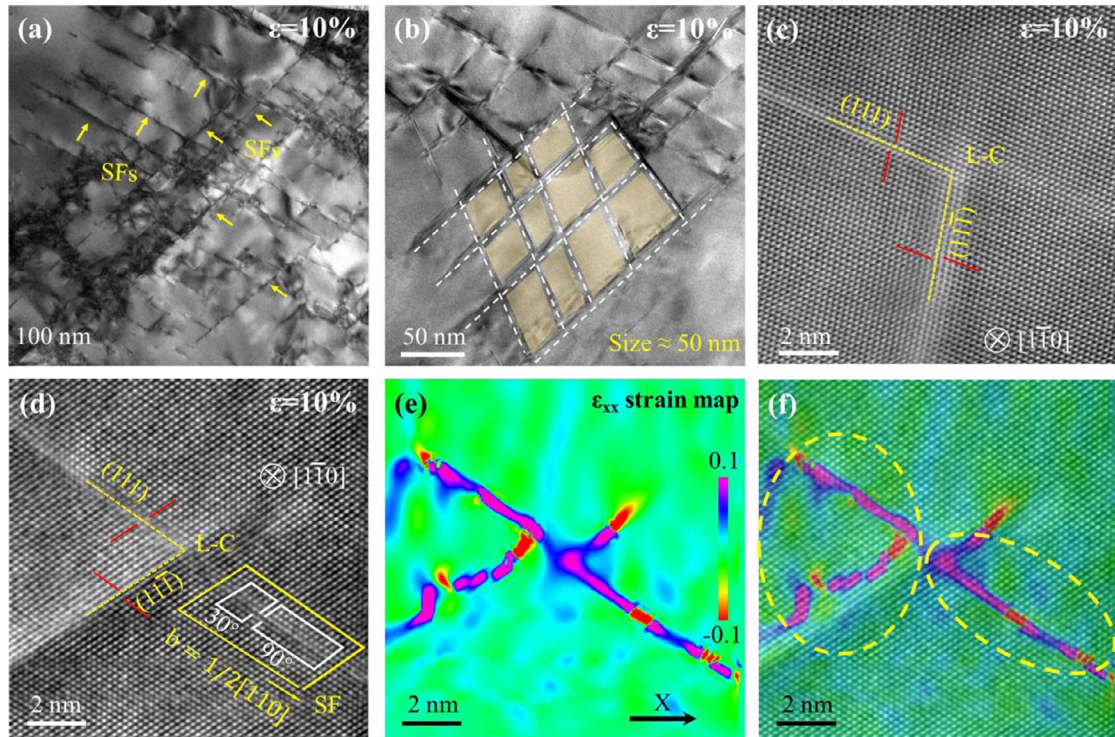


Fig. 7. Deformation mechanism in recrystallized grain in the RA-780 sample at 10% strain. (a) BF-STEM image showing a high density of stacking faults (marked by yellow arrows). (b) HAADF-STEM image revealing the stacking fault network structure (marked by white line). (c) High-resolution HAADF-STEM image showing the Lomer-Cottrell lock (labelled L-C). (d) HAADF-STEM image showing a Lomer-Cottrell lock and dislocation. (e) Distribution map of the horizontal lattice normal strain (ε_{xx}) of the area shown in (d). (f) The overlapped image of the HAADF-STEM image shown in (d) and the ε_{xx} strain map shown in (e).

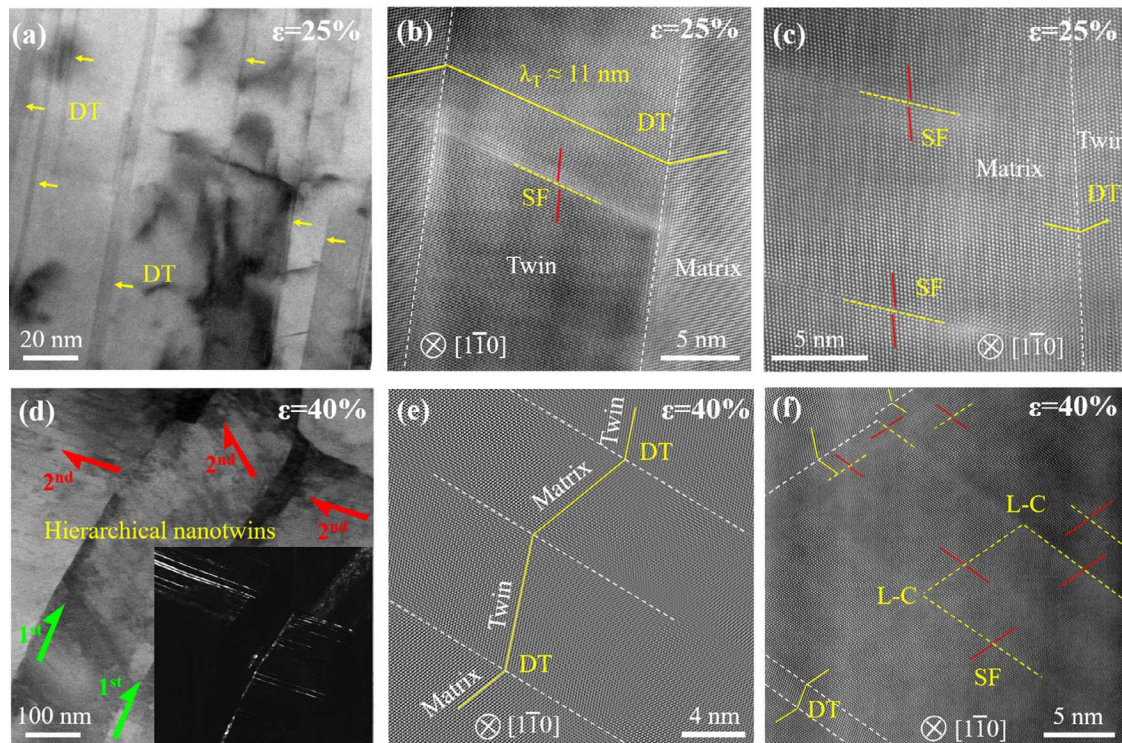


Fig. 8. Deformation mechanism in recrystallized grain in the RA-780 sample at different strains. Images were taken at strains of 25% for (a)-(c) and 40% for (d)-(f), as marked in the upper right corner of each. (a) HAADF-STEM image showing a high density of deformation twins (marked by yellow arrows). (b) and (c) HAADF-STEM images showing deformation twin and stacking faults. (d) HAADF-STEM image showing hierarchical nanotwins. The inset is the corresponding DF-TEM image. (e) HAADF-STEM image showing secondary deformation twins. (f) HAADF-STEM image showing secondary deformation twins, stacking faults and Lomer-Cottrell locks.

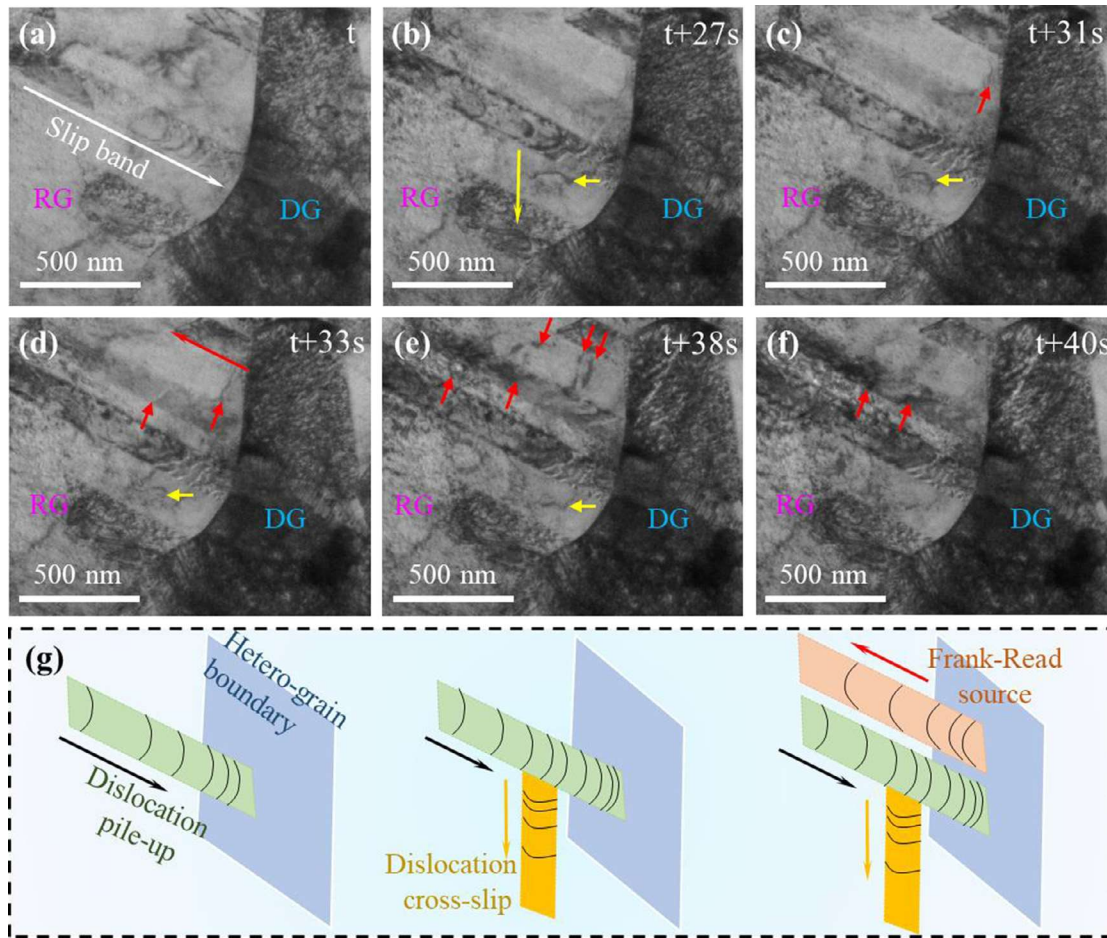


Fig. 9. TEM observation of dislocation motion in the heterostructured RA-780 sample during in situ deformation. (a) TEM image of an area containing one recrystallized grain (RG) and one deformation grain (DG) at an early stage of the in situ deformation. (b)-(f) Sequential TEM images of the same area at various stages of deformation. (g) Schematic illustration of the movement of dislocations within the vicinity of a hetero-grain boundary.

3.5. In situ micromechanisms of deformation in heterostructured RA-780

Fig. 9 shows an in situ TEM analysis of the microscopic deformation mechanisms in the heterostructured RA-780 sample. Fig. 9(a) shows a TEM image of a sample for in situ tensile deformation at one early moment of the deformation (denoted t). The viewing area contained one recrystallized grain and one deformed grain. A dislocation slip band had formed in the recrystallized grain. Figs. 9(b)-(f) show a series of TEM images of the same area taken at different times during the deformation process. With increased deformation, dislocations inside the recrystallized grain moved within the slip band and piled up in front of the boundary with the deformed grain. The deformed grain did not yield fresh dislocations but responded to the deformation only elastically (more clearly recognizable in Video S1), unlike what may be expected of a homo-grain boundary. This result demonstrates the effectiveness of hetero-deformation mechanism between recrystallized and deformed grains in the heterogeneous RA-780 sample. Some dislocations are also seen to have slipped out of the primary slip band, as indicated by the yellow arrows, signaling cross-slipping. Such cross-slip was enabled, or forced to occur, by the dislocation pile-ups, which exerted high back stresses on the dislocations following the primary slip plane and resisted their motion [66]. Furthermore, some dislocations were seen to emit from the hetero-grain boundary back into the recrystallized grain and moved away from the boundary, as indicated by the red arrows

in Figs. 9(c)-(e) and Video S1. This behavior indicates that the hetero-grain boundaries can act as Frank-Read dislocation sources. Fig. 9(g) schematically expresses the traces of the dislocation motion during tensile deformation.

4. Discussion

4.1. Stacking fault energy and critical stress for deformation twins

The plastic deformation mechanism of crystalline metallic materials includes dislocation, twinning, stacking fault, and phase transformation. In FCC-structured metallic materials, the way they deform is strongly correlated with their stacking fault energy [67]. In general, metallic materials with low stacking fault energy tend to deform by partial dislocation activities or twining, whereas those with high stacking fault energy tend to deform by full dislocation movement. According to experimental evidence and atomistic simulations reported in the literature, different microscopic mechanisms of deformation operate in different ranges of the stacking fault energy, as summarized in Table 1.

The stacking fault energy in a metal can be calculated using the following equation [68]:

$$\gamma = \frac{Gb^2}{8\pi\lambda_d} \left(\frac{2-\nu}{1-\nu} \right) \left(1 - \frac{2\nu\cos2\beta}{2-\nu} \right) \quad (5)$$

where G is the shear modulus, ν is Poisson's ratio, b is the magnitude of the Burgers vector of the partial dislocation, λ_d is the

Table 1

Stacking fault energy and deformation mechanism way for the crystalline metallic materials.

Stacking fault energy (SFE, mJ/m ²)	Deformation way			Ref
	Dislocation	Twinning	Phase transformation	
SFE<15~18	☒	☒	☒	[69]
~15<SFE<40	☒	☒		[70]
50<SFE	☒			[71]

average spacing between partial dislocations, and β is the angle between the Burgers vector of a perfect dislocation and the dislocation line. Based on the stress-strain curves, the Young's modulus of the $\text{Co}_{30}\text{Cr}_{20}\text{Fe}_{18}\text{Ni}_{14}\text{Mn}_{18}$ alloy was determined to be $E = 196.6$ GPa (Fig. 3(a)). Poisson's ratio is estimated to be 0.26 [33]. Thus, the shear modulus is determined to be $G = E/(2(1+\nu)) = 78$ GPa. The Burgers vector of partial dislocations was $b = \frac{a}{6}[112]$ for FCC metals and alloy. For the RA-780 sample, $a = 0.358$ nm and $b = 0.146$ nm. Based on the many HAADF-STEM images collected (Fig. 8), the λ_d was estimated to be ~ 11 nm. Using these values, the stacking fault energy (γ) of the $\text{Co}_{30}\text{Cr}_{20}\text{Fe}_{18}\text{Ni}_{14}\text{Mn}_{18}$ alloy is calculated to be 16.3 mJ/m².

Fig. S6 shows a comparison of the stacking fault energy for the $\text{Co}_{30}\text{Cr}_{20}\text{Fe}_{18}\text{Ni}_{14}\text{Mn}_{18}$ alloy with those of several widely studied FCC structured high- and medium-entropy alloys in the literature [33,66]. It is apparent that the RA-780 sample has the lowest stacking fault energy among these alloys.

Another factor determining whether twinning occurs is the relationship between the flow stress (σ_{flow}) and the critical stress for twinning (σ_{TW}) [34]. If $\sigma_{flow} > \sigma_{TW}$, twinning will be the dominant mechanism of deformation, and vice versa. The critical stress for twinning can be calculated as [72]:

$$\sigma_{TW} = M \left(\frac{\gamma}{3b} + \frac{3Gb}{L_0} \right) \quad (6)$$

where γ is the stacking fault energy, which is 16.3 mJ/m² for the $\text{Co}_{30}\text{Cr}_{20}\text{Fe}_{18}\text{Ni}_{14}\text{Mn}_{18}$ alloy, G is the shear modulus (78 GPa), L_0 is the width of the twin plates, which is assumed to be 260 nm [73], b is the magnitude of the Burgers vector of the partial dislocations (0.146 nm), and M is the Taylor factor, which is 3.06 for FCC metals. Accordingly, the critical stress for twinning in the $\text{Co}_{30}\text{Cr}_{20}\text{Fe}_{18}\text{Ni}_{14}\text{Mn}_{18}$ alloy is calculated to be 505 MPa for twinning. This value is lower than the yield stresses of the RA-730, RA-780 and RA-820 samples. As a result, it is reasonable to expect that deformation twinning will be activated at the onset of yielding in these three samples. The observation of deformation twins in the recrystallized grains in the RA-780 (Fig. 6(a)), RA-820 (Fig. S7) and RA-730 (Fig. S8) samples at 2% strain supports this calculation. In contrast, no deformation twins were observed in the homogenized sample in the early stages of deformation, but they were observed only at tensile strains above 25% (Fig. S9). This implies that $\sigma_{flow} > \sigma_{TW}$.

4.2. High strain hardening associated with heterogeneous structures

The RA-780 sample, which had a heterogeneous microstructure consisting of large "hard" deformation grains and small "soft" recrystallized grains, exhibited the highest strain hardening rate (Fig. 3(b)) and the best strength-ductility combination (Fig. 3(a)) among the four samples. The theoretical physics analysis work by Zhu et al. [25] attributed the high strain hardening of heterogeneous materials to the heterogeneous deformation between "soft" and "hard" regions. This is yet to be verified and supported by experimental evidence. The in situ TEM observation of this study reveals that the recrystallized grains deform first via dislocation move-

ment and form dislocation pile-ups at the hetero-grain boundaries. This causes high back stresses for the succeeding dislocations and thereby facilitates dislocation cross-slip. The cross-slip in turn causes dislocation interactions in adjacent slip bands, resulting in strain hardening. In an earlier study, dislocation cross-slip was also observed in a heterostructured HfNbTiV alloy, which exhibited a high strain hardening effect [63]. Recently, dislocation jogged and cross-slip were also reported for the cantor alloy with heterogeneous lattice field via high distorted lattice, facilitating dislocation interaction and accumulation, and thereby high strength and ductility [74]. In addition, dislocation pile-ups increase the strain fields in the vicinity of hetero-grain boundaries and stimulate Frank-Read dislocation sources. This contributes to a further increase in the dislocation density and dislocation interactions, thereby enhancing strain hardening.

On the other hand, the high strain hardening effect is also attributed to the co-occurrence of multiple deformation mechanisms within such a complex heterogeneous structure, including dislocation movement (Figs. 6a-c), stacking fault formation (Fig. 7) and twinning (Fig. 8). Fig. 10(a) shows a schematic diagram of the occurrence of the various deformation mechanisms during the deformation process. Previous study indicates that only deformation twins can improve the tensile ductility in two ways. First, twin boundaries can serve as an alternative way for dislocation sliding, and the presence of twins helps to mitigate stress localization, which is conducive to plastic deformation [65,67,75]. Second, the in situ stacking fault-deformation twin interaction can refine the mean free path of dislocations, facilitating strain hardening through the dynamic Hall-Petch effect [13,46]. Our results demonstrate that at different strains, the various structural elements, including grain boundaries, annealing twins, dislocations, stacking faults and deformation twins, effectively divide the larger grains into much smaller 'cage' for dislocation movement. Fig. 10(b) shows the distance for dislocation movement as a function of true strain. At the beginning of plasticity, the 'cage' is surrounded by grain boundaries (Type I, Fig. 1). At a strain of 2%, the 'cage' is enclosed by slip bands and dislocation columns (Type II, Fig. 6) whose refined size is about 800 nm. At a strain of 10%, the 'cage' is surrounded by stacking fault networks (Type III, Fig. 7) with a size of ~ 50 nm. As the strain increases to 25%, the 'cage' consists mainly of primary deformation twins (Type IV, Fig. 8) with a size of ~ 16.5 nm. When the strain reaches 40%, the 'cage' architecture becomes hierarchical deformation twins and stacking faults (Type V, Fig. 8) with a size of ~ 5 nm. As a result, the strain hardening effect was enhanced during tensile deformation via in situ refined of the mean free path of dislocation.

The progressive and sequential transition of the various strain hardening mechanisms in the RA-780 sample is unique in five aspects. First, the mean free path for dislocation movement becomes smaller with further deformation by the formation of Lomer-Cottrell locks and hierarchical deformation twins. This is facilitated by the synergistic effect of the low stacking fault energy of the $\text{Co}_{30}\text{Cr}_{20}\text{Fe}_{18}\text{Ni}_{14}\text{Mn}_{18}$ alloy and its high HDI hardening. Second, the hardening effect is operative even when the 'cage' size is reduced to 5 nm, overcoming the ceiling of the Hall-Petch effect, which is usually at ~ 15 nm of grain size [76]. As a result, the RA-780 sample exhibited a high strain hardening rate ($\theta = 2$ GPa) up to 35% true strain (Fig. 3(b)). Third, the strain hardening was not only enhanced by stacking faults and deformation twins but also enhanced by the interaction between dislocations and annealing twins (Fig. 6(c)) and between stacking faults (Fig. 7(f)) and deformation twins (Fig. 8(b)). Fourth, a high density of immobile dislocations and Lomer-Cottrell locks (Fig. 7) was formed in situ during the deformation process. Zhang et al. [77] argued that the effectiveness of Lomer-Cottrell locks in strain hardening stems from their ability to produce more dislocations.

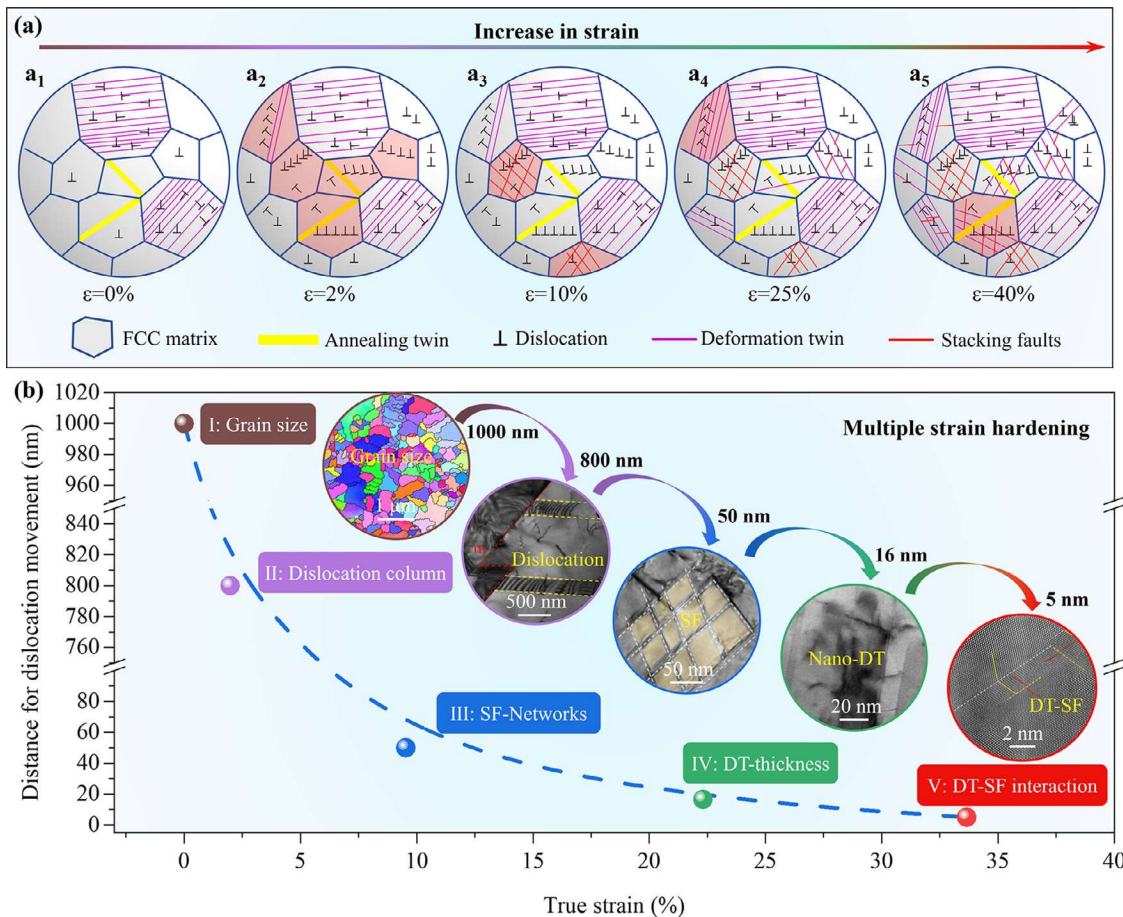


Fig. 10. Deformation mechanism and strain hardening mechanism of the RA-780 sample. (a) Schematic sketches illustrating the deformation mechanism transitions. (b) Multiple strain hardening mechanisms lead to in situ refinement of the dislocation mean free path.

Fifth, as shown in Fig. 8(a), a high density of secondary twins due to partial dislocation emissions from the other side of the twin boundary indicated that a high local strain energy was introduced by the accumulation of dislocations at the twin boundaries. This process accounts for the high density of dislocations, leading to a high strain hardening effect [78]. Recent studies also indicate that the Lomer-Cottrell locks and deformation twin boundaries can act as Frank-Read sources, which will also increase dislocation density [79,80]. Using the William-Hall method and high-energy synchrotron XRD [81,82], the dislocation density of the RA-780 sample at a tensile strain of 48% has been measured to be up to $1.28 \times 10^{15} \text{ m}^{-2}$. Han et al. [83] determined the dislocation densities in several heavily cold-worked metals by forging, including pure Ni, a binary NiFe alloy, a FeCoNi alloy and a CoCrFeNi-Mn HEA, to be in the range of $1.0 \times 10^{14} \sim 2.6 \times 10^{14} \text{ m}^{-2}$. In comparison, the dislocation density of the RA-780 sample is an order of magnitude higher. This may be due to the influences of the Lomer-Cottrell locks and deformation twins in preventing dislocation annihilation.

It is evident from the experimental observations and the analyses presented above that the RA-780 sample, which had a heterogeneous microstructure, exhibited distinctive deformation micromechanisms different from both the comparison materials tested in this study and the conventional heterogeneous structure alloys reported in the literature. This is directly related to the concurrent effects of the low stacking fault energy and the heterogeneous structure. This gave the alloy a high strain hardening capability and thus an excellent combined strength-ductility performance. In this regard, this study not only enables the design

and development of high-performance high entropy alloys but also helps to advance the fundamental understanding of the chemical composition-structure-property relationships of these alloys.

5. Conclusions

This study investigated a new alloy design strategy to achieve high strength and ductility by incorporating heterogeneous structures into a low stacking fault energy alloy. The findings lead to the following conclusions.

- (1) The $\text{Co}_{30}\text{Cr}_{20}\text{Fe}_{18}\text{Ni}_{14}\text{Mn}_{18}$ composition design allows the stacking fault energy to be reduced to 16.3 mJ/m^2 , by 61% relative to its equiatomic counterpart.
- (2) Heat treating the alloy at 780°C for 10 min produces a heterogeneous microstructure consisting of microscale grain structure heterogeneity and nanoscale defect heterogeneity of dislocations, stacking faults, deformed twins and annealing twins.
- (3) As a result, the alloy with the heterogeneous microstructure exhibited a yield strength of 980 MPa, an ultimate tensile strength of 1380 MPa and a tensile elongation to failure of $\sim 48\%$. The high yield strength is mainly attributed to heterogeneous deformation induced strengthening, which is estimated to be 561 MPa.
- (4) The high combined strength-ductility performance of the RA-780 sample is attributed to its high strain hardening rate caused by HDI hardening, stacking fault formation and deformation twinning. The underlying reason for HDI hardening can be ascribed to dislocation pile-up, cross-slip and

activate the dislocation source. The sequential activation of these mechanisms and the interactions among them lead to a gradually refined dislocation mean free path and continued strain hardening during deformation, which helped to prevent early necking and thus sample rupture.

- (5) A high density of Lomer–Cottrell locks was formed. These locks cause lattice strains and retard dislocation motion and thereby facilitate dislocation multiplication and accumulation. This provides additional hardening for the RA-780 sample.

Declaration of Competing Interest

The authors declare that they have no known competing financial interests or personal relationships that could have appeared to influence the work reported in this paper.

Acknowledgements

This research was supported by the National Key R&D Program of China ([2021YFA1200201](#)), Natural Science Foundation of China ([52071003](#), [91860202](#)), Beijing Nova Program ([Z211100002121170](#)), Beijing Municipal Education Commission Project ([PXM2020_014204_000021](#)), Beijing Outstanding Young Scientists Projects ([BJJWZYJH01201910005018](#)), and “111” project ([DB18015](#)).

Supplementary materials

Supplementary material associated with this article can be found, in the online version, at [doi:10.1016/j.actamat.2022.118516](https://doi.org/10.1016/j.actamat.2022.118516).

References

- [1] J.W. Yeh, S.K. Chen, S.J. Lin, J.Y. Gan, T.S. Chin, T.T. Shun, C.H. Tsau, S.Y. Chang, Nanostructured high-entropy alloys with multiple principal elements: novel alloy design concepts and outcomes, *Adv. Eng. Mater.* 6 (2004) 299–303.
- [2] B. Cantor, I.T.H. Chang, P. Knight, A.J.B. Vincent, Microstructural development in equiatomic multicomponent alloys, *Mater. Sci. Eng A* 375–377 (2004) 213–218.
- [3] E.P. George, D. Raabe, R.O. Ritchie, High-entropy alloys, *Nat. Rev. Mater.* 4 (2019) 515–534.
- [4] W.D. Li, D. Xie, Y. Zhang, Y.F. Gao, P.K. Liaw, Mechanical behavior of high-entropy alloys, *Prog. Mater. Sci.* 118 (2020) 100777.
- [5] Q.F. He, J.G. Wang, H.A. Chen, Z.Y. Ding, Z.Q. Zhou, L.H. Xiong, J.H. Luan, J.M. Pelletier, J.C. Qiao, Q. Wang, L.L. Fan, Y. Ren, Q.S. Zeng, C.T. Liu, C.W. Pao, D.J. Srolovitz, Y. Yang, A highly distorted ultralastic chemically complex Elinvar alloy, *Nature* 602 (2022) 251–257.
- [6] B. Gludovatz, A. Hohenwarter, D. Catoor, E.H. Chang, E.P. George, R.O. Ritchie, A fracture-resistant high-entropy alloy for cryogenic applications, *Science* 345 (2014) 1153–1158.
- [7] Z. Zhang, M.M. Mao, J. Wang, B. Gludovatz, Z. Zhang, S.X. Mao, E.P. George, Q. Yu, R.O. Ritchie, Nanoscale origins of the damage tolerance of the high-entropy alloy CrMnFeCoNi, *Nat. Commun.* 6 (2015) 10143.
- [8] C. Wagner, A. Ferrari, J. Schreuer, J.P. Couzinié, Y. Ikeda, F. Körmann, G. Eggeler, E.P. George, G. Laplanche, Effects of Cr/Ni ratio on physical properties of Cr-Mn-Fe-Co-Ni high-entropy alloys, *Acta Mater.* 227 (2022) 117693.
- [9] R. Daniel, J. Zalesak, I. Matko, W. Baumegger, A. Hohenwarter, E.P. George, J. Keckes, Microstructure-dependent phase stability and precipitation kinetics in equiatomic CrMnFeCoNi high-entropy alloy: role of grain boundaries, *Acta Mater.* 223 (2022) 117470.
- [10] B. Cantor, Multicomponent high-entropy Cantor alloys, *Prog. Mater. Sci.* 120 (2020) 100754.
- [11] G. Laplanche, A. Kostka, O.M. Horst, G. Eggeler, E.P. George, Microstructure evolution and critical stress for twinning in the CrMnFeCoNi high-entropy alloy, *Acta Mater.* 118 (2016) 152–163.
- [12] M. Laurent-Brocq, A. Akhatova, L. Perrière, S. Chebini, X. Sauvage, E. Leroy, Y. Champion, Insights into the phase diagram of the CrMnFeCoNi high entropy alloy, *Acta Mater.* 88 (2015) 355–365.
- [13] Y. Deng, C.C. Tasan, K.G. Pradeep, H. Springer, A. Kostka, D. Raabe, Design of a twinning-induced plasticity high entropy alloy, *Acta Mater.* 94 (2015) 124–133.
- [14] J.C. Rao, H.Y. Diao, V. Ocelík, D. Vainchtein, C. Zhang, C. Kuo, Z. Tang, W. Guo, J.D. Poplawsky, Y. Zhou, P.K. Liaw, J.T.M. De Hosson, Secondary phases in Al \times CoCrFeNi high-entropy alloys: an in-situ TEM heating study and thermodynamic appraisal, *Acta Mater.* 131 (2017) 206–220.
- [15] W.H. Liu, Z.P. Lu, J.Y. He, J.H. Luan, Z.J. Wang, B. Liu, Y. Liu, M.W. Chen, C.T. Liu, Ductile CoCrFeNiMox high entropy alloys strengthened by hard intermetallic phases, *Acta Mater.* 116 (2016) 332–342.
- [16] F. Otto, A. Dlouhý, C. Somsen, H. Bei, G. Eggeler, E.P. George, The influences of temperature and microstructure on the tensile properties of a CoCrFeMnNi high-entropy alloy, *Acta Mater.* 61 (2013) 5743–5755.
- [17] Z. Wu, H. Bei, G.M. Pharr, E.P. George, Temperature dependence of the mechanical properties of equiatomic solid solution alloys with face-centered cubic crystal structures, *Acta Mater.* 81 (2014) 428–441.
- [18] B. Gwalani, V. Soni, M. Lee, S.A. Mantri, Y. Ren, R. Banerjee, Optimizing the coupled effects of Hall-Petch and precipitation strengthening in a Al 0.3 CoCrFeNi high entropy alloy, *Mater. Des.* 121 (2017) 254–260.
- [19] I.S. Wani, T. Bhattacharjee, S. Sheikh, I.T. Clark, M.H. Park, T. Okawa, S. Guo, P.P. Bhattacharjee, N. Tsuji, Cold-rolling and recrystallization textures of a nano-lamellar AlCoCrFeNi2.1 eutectic high entropy alloy, *Intermetallics* 84 (2017) 42–51.
- [20] M.J. Yao, K.G. Pradeep, C.C. Tasan, D. Raabe, A novel, single phase, non-equiatomic FeMnNiCoCr high-entropy alloy with exceptional phase stability and tensile ductility, *Scr. Mater.* 72–73 (2014) 5–8.
- [21] W. Jiang, Y. Zhu, Y. Zhao, Mechanical properties and deformation mechanisms of heterostructured high-entropy and medium-entropy alloys: a review, *Front. Mater.* 8 (2022) 792359.
- [22] J. Moon, E. Tabachnikova, S. Shumilin, T. Hryhorova, Y. Estrin, J. Brecht, P.K. Liaw, W. Wang, K.A. Dahmen, A. Zargaran, J.W. Bae, H.S. Do, B.J. Lee, H.S. Kim, Deformation behavior of a Co-Cr-Fe-Ni-Mo medium-entropy alloy at extremely low temperatures, *Mater. Today* 50 (2021) 55–68.
- [23] P. Sathiyanamoorthi, H.S. Kim, High-entropy alloys with heterogeneous microstructure: processing and mechanical properties, *Prog. Mater. Sci.* 123 (2020) 100709.
- [24] E. Ma, Y.T. Zhu, Towards strength-ductility synergy through the design of heterogeneous nanostructures in metals, *Mater. Today* 20 (2017) 323–331.
- [25] Y.T. Zhu, X.L. Wu, Perspective on hetero-deformation induced (HDI) hardening and back stress, *Mater. Res. Lett.* 7 (2019) 393–398.
- [26] X.L. Wu, Y.T. Zhu, Gradient and lamellar heterostructures for superior mechanical properties, *MRS Bull.* 46 (2021) 244–249.
- [27] E. Ma, X.L. Wu, Tailoring heterogeneities in high-entropy alloys to promote strength-ductility synergy, *Nat. Commun.* 10 (2019) 5623.
- [28] X.L. Wu, M.X. Yang, F.P. Yuan, G.L. Wu, Y.J. Wei, X.X. Huang, Y.T. Zhu, Heterogeneous lamella structure unites ultrafine-grain strength with coarse-grain ductility, *Proc. Natl. Acad. Sci.* 112 (2015) 14501–14505.
- [29] M.X. Yang, D.S. Yan, F.P. Yuan, P. Jiang, E. Ma, X.L. Wu, Dynamically reinforced heterogeneous grain structure prolongs ductility in a medium-entropy alloy with gigapascal yield strength, *Proc. Natl. Acad. Sci.* 115 (2018) 7224–7229.
- [30] S.W. Wu, G. Wang, Q. Wang, Y.D. Jia, J. Yi, Q.J. Zhai, J.B. Liu, B.A. Sun, H.J. Chu, J. Shen, P.K. Liaw, C.T. Liu, T.Y. Zhang, Enhancement of strength-ductility trade-off in a high-entropy alloy through a heterogeneous structure, *Acta Mater.* 165 (2019) 444–458.
- [31] N.L. Okamoto, K. Yuge, K. Tanaka, H. Inui, E.P. George, Atomic displacement in the CrMnFeCoNi high-entropy alloy – a scaling factor to predict solid solution strengthening, *AIP Adv.* 6 (2016) 125008.
- [32] G. Laplanche, S. Berglund, C. Reinhart, A. Kostka, F. Fox, E.P. George, Phase stability and kinetics of σ -phase precipitation in CrMnFeCoNi high-entropy alloys, *Acta Mater.* 161 (2018) 338–351.
- [33] S.F. Liu, Y. Wu, H.T. Wang, J.Y. He, J.B. Liu, C.X. Chen, X.J. Liu, H. Wang, Z.P. Lu, Stacking fault energy of face-centered-cubic high entropy alloys, *Intermetallics* 93 (2018) 269–273.
- [34] Z.B. An, S.C. Mao, Y.N. Liu, H. Zhou, Y.D. Zhai, Z.Y. Tian, C.X. Liu, Z. Zhang, X.D. Han, Hierarchical grain size and nanotwin gradient microstructure for improved mechanical properties of a non-equiatomic CoCrFeMnNi high-entropy alloy, *J. Mater. Sci. Technol.* 92 (2021) 195–207.
- [35] B.S. Lee, Y. Koizumi, H. Matsumoto, A. Chiba, Collective behavior of strain-induced martensitic transformation (SIMT) in biomedical Co–Cr–Mo–N alloy polycrystal: an ex-situ electron backscattering diffraction study, *Mater. Sci. Eng. A* 611 (2014) 263–273.
- [36] Y. Zhang, Y.J. Zhou, J.P. Lin, G.L. Chen, P.K. Liaw, Solid-solution phase formation rules for multi-component alloys, *Adv. Eng. Mater.* 10 (2008) 534–538.
- [37] X. Chang, M. Zeng, K. Liu, L. Fu, Phase Engineering of High-Entropy Alloys, *Adv. Mater.* 32 (2020) 1907226.
- [38] Y. Zhang, Y.J. Zhou, J.P. Lin, G.L. Chen, P.K. Liaw, Solid-Solution Phase Formation Rules for Multi-component Alloys, *Adv. Eng. Mater.* 10 (2008) 534–538.
- [39] Y. Zhang, Z.P. Lu, S.G. Ma, P.K. Liaw, Z. Tang, Y.Q. Cheng, M.C. Gao, Guidelines in predicting phase formation of high-entropy alloys, *MRS Commun.* 4 (2014) 57–62.
- [40] N. Saunders, U.K.Z. Guo, X. Li, A.P. Miodownik, J.P. Schillé, Using JMatPro to Model Materials Properties and Behavior, *JOM* 55 (2003) 60–65.
- [41] C. Lee, G. Song, M.C. Gao, R. Feng, P. Chen, J. Brecht, Y. Chen, K. An, W. Guo, J.D. Poplawsky, S. Li, A.T. Samaei, W. Chen, A. Hu, H. Choo, P.K. Liaw, Lattice distortion in a strong and ductile refractory high-entropy alloy, *Acta Mater.* 160 (2018) 158–172.
- [42] M.C. Gao, C.S. Carney, Ö.N. Doğan, P.D. Jablonksi, J.A. Hawk, D.E. Alman, Design of refractory high-entropy alloys, *JOM* 67 (2015) 2653–2669.
- [43] L.P. Kubin, A. Mortensen, Geometrically necessary dislocations and strain-gradient plasticity: a few critical issues, *Scr. Mater.* 48 (2003) 119–125.
- [44] T. Yang, Y.L. Zhao, Y. Tong, Z.B. Jiao, J. Wei, J.X. Cai, X.D. Han, D. Chen, A. Hu, J.J. Kai, K. Lu, Y. Liu, C.T. Liu, Multicomponent intermetallic nanoparticles and superb mechanical behaviors of complex alloys, *Science* 362 (2018) 933–937.
- [45] P.J. Shi, W. Ren, T.X. Zheng, Z.M. Ren, X.L. Hou, J.C. Peng, P.F. Hu, Y.F. Gao, Y.B. Zhong, P.K. Liaw, Enhanced strength-ductility synergy in ultrafine-grained

- eutectic high-entropy alloys by inheriting microstructural lamellae, *Nat. Commun.* 10 (2019) 1–8.
- [46] Z.M. Li, K.G. Pradeep, Y. Deng, D. Raabe, C.C. Tasan, Metastable high-entropy dual-phase alloys overcome the strength-ductility trade-off, *Nature* 534 (2016) 227–230.
- [47] H. Huang, Y. Wu, J. He, H. Wang, X. Liu, K. An, W. Wu, Z. Lu, Phase-Transformation Ductilization of Brittle High-Entropy Alloys via Metastability Engineering, *Adv. Mater.* 29 (2017) 1701678.
- [48] L. Liliensten, J.P. Couzinié, J. Bourgon, L. Perrière, G. Dirras, F. Prima, I. Guillot, Design and tensile properties of a bcc Ti-rich high-entropy alloy with transformation-induced plasticity, *Mater. Res. Lett.* 5 (2016) 110–116.
- [49] Y.D. Wu, Y.H. Cai, T. Wang, J.J. Si, J. Zhu, Y.D. Wang, X.D. Hui, A refractory Hf₂₅Nb₂₅Ti₂₅Zr₂₅ high-entropy alloy with excellent structural stability and tensile properties, *Mater. Lett.* 130 (2014) 277–280.
- [50] O.N. Senkov, S.L. Semiatin, Microstructure and properties of a refractory high-entropy alloy after cold working, *J. Alloys Compd.* 649 (2015) 1110–1123.
- [51] G. Dirras, L. Liliensten, P. Djemla, M. Laurent-Brocq, D. Tingaud, J.P. Couzinié, L. Perrière, T. Chauveau, I. Guillot, Elastic and plastic properties of as-cast equimolar TiHfZrTaNb high-entropy alloy, *Mater. Sci. Eng. A* 654 (2016) 30–38.
- [52] S. Sheikh, S. Shafeie, Q. Hu, J. Ahlström, C. Persson, J. Veselý, J. Zýka, U. Klement, S. Guo, Alloy design for intrinsically ductile refractory high-entropy alloys, *J. Appl. Phys.* 120 (2016) 164902.
- [53] J.Y. He, H. Wang, Y. Wu, X.J. Liu, H.H. Mao, T.G. Nieh, Z.P. Lu, Precipitation behavior and its effects on tensile properties of FeCoNiCr high-entropy alloys, *Intermetallics* 79 (2016) 41–52.
- [54] Z. Wang, I. Baker, Effects of annealing and thermo-mechanical treatment on the microstructures and mechanical properties of a carbon-doped FeNiMnAl multi-component alloy, *Mater. Sci. Eng. A Struct. Mater.* 693 (2017) 101–110.
- [55] Y. Dong, X. Gao, Y.P. Lu, T.M. Wang, T.J. Li, A multi-component AlCrFe2Ni2 alloy with excellent mechanical properties, *Mater. Lett.* 169 (2016) 62–64.
- [56] Y.M. Wang, M.W. Chen, F.H. Zhou, E. Ma, High tensile ductility in a nanostructured metal, *Nature* 419 (2002) 912–915.
- [57] E. Ma, Eight Routes to Improve the Tensile Ductility of Bulk Nanostructured Metals and Alloys, *JOM* 58 (2006) 49–53.
- [58] Y. Zhu, K. Ameyama, P.M. Anderson, I.J. Beyerlein, H. Gao, H.S. Kim, E. Lavernia, S. Mathaudhu, H. Mughrabi, R.O. Ritchie, N. Tsuji, X. Zhang, X. Wu, Heterostructured materials: superior properties from hetero-zone interaction, *Mater. Res. Lett.* 9 (2020) 1–31.
- [59] M. Yang, Y. Pan, F. Yuan, Y. Zhu, X. Wu, Back stress strengthening and strain hardening in gradient structure, *Mater. Res. Lett.* 4 (2016) 145–151.
- [60] Z. Zhang, W. Wang, S. Qin, M. Yang, J. Wang, P. Jiang, F. Yuan, X. Wu, Dual heterogeneous structured medium-entropy alloys showing a superior strength-ductility synergy at cryogenic temperature, *J. Mater. Res. Technol.* 17 (2022) 3262–3276.
- [61] Q.S. Pan, L.X. Zhang, R. Feng, Q.H. Lu, K. An, A.C. Chuang, J.D. Poplawsky, P.K. Liaw, L. Lu, Gradient-cell-structured high-entropy alloy with exceptional strength and ductility, *Science* 374 (2021) 984–989.
- [62] M.N. Hasan, Y.F. Liu, X.H. An, J. Gu, M. Song, Y. Cao, Y.S. Li, Y.T. Zhu, X.Z. Liao, Simultaneously enhancing strength and ductility of a high-entropy alloy via gradient hierarchical microstructures, *Int. J. Plast.* 123 (2019) 178–195.
- [63] Z. An, S. Mao, T. Yang, C.T. Liu, B. Zhang, E. Ma, H. Zhou, Z. Zhang, L. Wang, X. Han, Spinodal-modulated solid solution delivers a strong and ductile refractory high-entropy alloy, *Mater. Horiz.* 8 (2021) 948–955.
- [64] H. Li, H. Zong, S. Li, S. Jin, Y. Chen, M.J. Cabral, B. Chen, Q. Huang, Y. Chen, Y. Ren, K. Yu, S. Han, X. Ding, G. Sha, J. Lian, X. Liao, E. Ma, J. Sun, Uniting tensile ductility with ultrahigh strength via composition undulation, *Nature* 604 (2022) 273–279.
- [65] L. Wang, Y. Lu, D. Kong, L. Xiao, X. Sha, J. Sun, Z. Zhang, X. Han, Dynamic and atomic-scale understanding of the twin thickness effect on dislocation nucleation and propagation activities by *in situ* bending of Ni nanowires, *Acta Mater.* 90 (2015) 194–203.
- [66] Q. Ding, Y. Zhang, X. Chen, X. Fu, D. Chen, S. Chen, L. Gu, F. Wei, H. Bei, Y. Gao, M. Wen, J. Li, Z. Zhang, T. Zhu, R.O. Ritchie, Q. Yu, Tuning element distribution, structure and properties by composition in high-entropy alloys, *Nature* 574 (2019) 223–227.
- [67] Z. He, N. Jia, H. Yan, Y. Shen, M. Zhu, X. Guan, X. Zhao, S. Jin, G. Sha, Y. Zhu, C.T. Liu, Multi-heterostructure and mechanical properties of N-doped FeMn-CoCr high entropy alloy, *Int. J. Plast.* 139 (2021) 102965.
- [68] R. Zhang, S. Zhao, J. Ding, Y. Chong, T. Jia, C. Ophus, M. Asta, R.O. Ritchie, A.M. Minor, Short-range order and its impact on the CrCoNi medium-entropy alloy, *Nature* 581 (2020) 283–287.
- [69] D. Wei, X. Li, S. Schönecker, J. Jiang, W.M. Choi, B.J. Lee, H.S. Kim, A. Chiba, H. Kato, Development of strong and ductile metastable face-centered cubic single-phase high-entropy alloys, *Acta Mater.* 181 (2019) 318–330.
- [70] S. Curtze, V.T. Kuokkala, Dependence of tensile deformation behavior of TWIP steels on stacking fault energy, temperature and strain rate, *Acta Mater.* 58 (2010) 5129–5141.
- [71] S. Chen, R. Rana, A. Haldar, R.K. Ray, Current state of Fe-Mn-Al-C low density steels, *Prog. Mater. Sci.* 89 (2017) 345–391.
- [72] S. Mahajan, C.S. Pande, M.A. Imam, B.B. Rath, Formation of annealing twins in f.c.c. crystals, *Acta Mater.* 45 (1997) 2633–2638.
- [73] J. Su, D. Raabe, Z. Li, Hierarchical microstructure design to tune the mechanical behavior of an interstitial TRIP-TWIP high-entropy alloy, *Acta Mater.* 163 (2019) 40–54.
- [74] J. Li, Y. Chen, Q. He, X. Xu, H. Wang, C. Jiang, B. Liu, Q. Fang, Y. Liu, Y. Yang, P.K. Liaw, C.T. Liu, Heterogeneous lattice strain strengthening in severely distorted crystalline solids, *Proc. Natl. Acad. Sci.* 119 (2022) 2200607119.
- [75] Z. Cheng, H. Zhou, Q. Lu, H. Gao, L. Lu, Extra strengthening and work hardening in gradient nanotwinned metals, *Science* 362 (2018) eaau1925.
- [76] J. Hu, Y.N. Shi, X. Sauvage, G. Sha, K. Lu, Grain boundary stability governs hardening and softening in extremely fine nanogranular metals, *Science* 355 (2017) 1292–1296.
- [77] D.D. Zhang, J.Y. Zhang, J. Kuang, G. Liu, J. Sun, Superior strength-ductility synergy and strain hardenability of Al/Ta co-doped NiCoCr twinned medium entropy alloy for cryogenic applications, *Acta Mater.* 220 (2021) 117288.
- [78] S. Ni, Y.B. Wang, X.Z. Liao, R.B. Figueiredo, H.Q. Li, S.P. Ringer, T.G. Langdon, Y.T. Zhu, The effect of dislocation density on the interactions between dislocations and twin boundaries in nanocrystalline materials, *Acta Mater.* 60 (2012) 3181–3189.
- [79] X.L. Wu, Y.T. Zhu, Y.G. Wei, Q. Wei, Strong strain hardening in nanocrystalline nickel, *Phys. Rev. Lett.* 103 (2009) 205504.
- [80] L. Fan, T. Yang, Y. Zhao, J. Luan, G. Zhou, H. Wang, Z. Jiao, C.T. Liu, Ultrahigh strength and ductility in newly developed materials with coherent nanolamellar architectures, *Nat. Commun.* 11 (2020) 1–8.
- [81] G. Dini, R. Ueji, A. Najafizadeh, S.M. Monir-Vaghefi, Flow stress analysis of TWIP steel via the XRD measurement of dislocation density, *Mater. Sci. Eng. A* 527 (2010) 2759–2763.
- [82] R.E. Smallman, K.H. Westmacott, Stacking faults in face-centred cubic metals and alloys, *Philos. Mag.* 2 (1957) 669–683.
- [83] P. Thirathipviwat, G. Song, J. Bednarcik, U. Kühn, T. Gemming, K. Nielsch, J. Han, Compositional complexity dependence of dislocation density and mechanical properties in high entropy alloy systems, *Prog. Nat. Sci.* 30 (2020) 545–551.